Journal of Alloys and Compounds 984 (2024) 173985

Contents lists available at ScienceDirect

Journal of Alloys and Compounds

journal homepage: www.elsevier.com/locate/jalcom

Research article

Comparative drawability and recrystallization evaluation of Nb4Ta and Nb4Ta1Hf alloys, and the beneficial influence of Hf on developing finer Nb_3Sn grain size

Shreyas Balachandran [a,*], Benjamin Walker [a,b], Peter J. Lee [a], William L. Starch [a], Chiara Tarantini [a], David C. Larbalestier [a,b,**]

[a] Applied Superconductivity Center, NHMFL, Tallahassee, FL 32309, USA
[b] Department of Mechanical Engineering, FAMU-FSU College of Engineering, Tallahassee, FL 32309, USA

ARTICLE INFO

Keywords:
Nb_3Sn conductors
Nb alloys
Drawability
Irreversibility fields

ABSTRACT

Nb_3Sn superconducting wires with high critical current density (J_c, 4.2 K) at fields greater than 15 T are needed for next-generation superconducting magnets for high-energy physics and nuclear magnetic resonance applications. It has been demonstrated that the addition of one atomic % Hf can significantly increase the high field J_c of Ta-doped Nb_3Sn and offer the potential to meet the Future Circular Collider (FCC) specification of 1500 A/mm^2 at 16 T, 4.2 K if the pure Nb filaments in conventional Nb_3Sn composites can be replaced by Nb4Ta1Hf alloy. In this paper we demonstrate that a commercially produced Nb4Ta1Hf alloy is ductile and drawable in a Cu matrix to a large true strain of 15 without intermediate annealing. The hardness and work-hardening rates of Nb4Ta1Hf are shown to be higher than Nb and commercial Nb4Ta, but are comparable to ductile Nb47Ti alloy at high strains, which is significant because more than 1000 tons of Nb-Ti rods are co-drawn in Cu each year. Very importantly for the Nb_3Sn properties is that just 1 at%Hf shifts the recrystallization curve of Nb4Ta to temperatures above the normal 600 °C –700 °C A15 range of reaction temperatures used for Nb_3Sn wires. For the Hf-based 19 filament rod in tube (RIT) conductors of this study, we observe a refined (<100 nm) Nb_3Sn grain size, and an improved upper critical field of 24.6 T (4.2 K), ~1 T higher than that in a corresponding Nb4Ta composite. The demonstration of improved performance and good drawability with commercially produced Nb4Ta1Hf alloy indicates a pathway for Nb_3Sn strand development for next-generation Nb_3Sn magnets.

1. Introduction

High critical current density (J_c) Nb_3Sn superconducting wires are needed to upgrade compact bending and aperture magnets, typically used but not limited to high energy physics applications involving accelerators and beams [1], [2]. For instance, the Future Circular Collider (FCC) that would succeed the Large Hadron Collider would be a ~ 100 TeV proton-proton collider [3] for which advanced Nb_3Sn wires are an essential, enabling technology. A key milestone has been the production of 11–12 T dipole Nb_3Sn magnets for the LHC's high luminosity upgrade (HL-LHC) [4], with fabricated prototypes of the quadrupole magnets MQXFB showing performance of over 90% of the nominal current requirement [5], [6]. These first Nb_3Sn accelerator magnets use commercially available Ti-doped Nb_3Sn superconductors developed for accelerator applications [7], and have two layers of coil blocks but a recent prototype with 4 layers in a cosine theta design enabled a 14 T dipole [8].

The demanding requirements of the Nb_3Sn dipole and quadrupole magnets for the HL-LHC project saw extensive development of the established RRP and PIT as well as some new wire designs [9], [10], conductor level specifications of Sn levels [11], and heat treatment control [12], [13]. However, meeting the demanding FCC requirements will require significantly higher performance than the best Nb_3Sn production superconductors. The desired target has been set at a non-Cu J_c of 1500 A/mm^2 at 16 T (4.2 K) with an effective filament diameter d_{eff} of less than 20 µm, keeping a residual resistivity ratio of the Cu matrix larger than 150 [14]. New routes to developing long-length, high J_c Nb_3Sn conductors must be investigated to meet this challenge.

---

* Corresponding author.
** Corresponding author at: Department of Mechanical Engineering, FAMU-FSU College of Engineering, Tallahassee, FL 32309, USA.
E-mail addresses: shreyas@jlab.org (S. Balachandran), larbalestier@asc.magnet.fsu.edu (D.C. Larbalestier).

https://doi.org/10.1016/j.jallcom.2024.173985
Received 13 December 2022; Received in revised form 20 February 2024; Accepted 24 February 2024
Available online 25 February 2024

High J_c values at high fields in Nb_3Sn require homogenously high Sn levels in the Nb_3Sn, Ti or Ta doping to achieve high irreversibility fields [15], and a high density of flux pinning sites. The dominant flux pinning sites in conventional Nb_3Sn are grain boundaries, so refining the grain size is an important path to raising J_c [16]. Artificial pinning center (APCs) designs have also been shown to be effective in increasing the J_c in lab- and pilot-scale wires where 1Zr is added to the Nb alloy and internally oxidized to make ZrO_2 that can add both oxide point pinning and refine the A15 grain size[17], [18]. In recent APC conductors both oxide pinning centers, and grain refinement may be in play [19]. Hf also has the potential to form oxide precipitates like Zr and we have pursued the grain refinement route with Hf additions, which also have the potential to increase the irreversibility field. In particular, we found that the addition of Hf to an Nb-4at%Ta (Nb4Ta) alloy improved the pinning performance sufficiently to raise the layer J_c at 16 T (4.2 K) beyond the FCC specification in a demonstrative monofilament wire [20]. The Nb_3Sn formed during the reaction heat treatment of this new Nb-4at% Ta-1at%Hf (Nb4Ta1Hf) alloy with no SnO_2 additions had an approximately halved grain size of order 70–100 nm and nanometer-scale HfO_2 precipitates, which together gave both point-pinning and grain-boundary pinning contributions to the increased J_c [21]. A key finding of our exploration of this new alloy is that the addition of Hf to Nb4Ta delays the recrystallization seen in the binary alloy [22]. The refined grain size of the Nb4Ta1Hf alloy during the A15 reaction heat treatment produced a much higher density of nucleated Nb_3Sn grains at the interface with the Nb4Ta1Hf alloy. We proposed that the retained cold-worked microstructure resulted in better Sn diffusion and denser heterogeneous nucleation of more refined Nb_3Sn grains, improving vortex pinning performance at high fields.

APC conductors using PIT routes with NbTaZr, and NbTaHf tubes are being fabricated using strategies that combine SnO_2 powder with the precursor Sn to provide the source oxygen for oxide formation [18], [19], [23], [24]. Beyond PIT methods, ternary additions of Nb-Ta-Zr/Hf are being pursued in other internal-tin configurations showing promising results in increasing J_c at 16 T and 4.2 K [25], [26]; this was enabled by enhanced vortex pinning dominated by GBs with no second phases, providing additional paths to achieve high performance in next generation Nb_3Sn conductors.

However, developing km lengths of Nb_3Sn strands needed for magnet cables requires the ability to make multi-filament composite conductors in which the filaments are uniformly drawn down to diameters as small as 2–3 µm. In this paper, we focus on the drawability of the Nb4Ta1Hf alloy to large strains, and we evaluate the recrystallization behavior of commercial alloy compared to a standard commercial Nb4Ta alloy.

To address these issues this paper seeks to answer the following questions:

1. Is Nb4Ta1Hf alloy drawable to large strains and fine filaments in a Cu matrix? How does the drawability compare to that of a standard Nb4Ta alloy?
2. How does the addition of 1 at% Hf affect the recrystallization and grain growth characteristics of the standard Nb4Ta alloy?

We conclude by presenting superconducting characterizations of RIT (rod-in-tube) conductors fabricated with commercial Nb4Ta1Hf and Nb4Ta alloys and investigate the influence of Hf on the Nb_3Sn properties, especially the Nb_3Sn grain size and irreversibility field.

2. Experimental details

2.1. Description of raw material

The alloys investigated here included in-house, arc-melted, lab-scale buttons made into rods, as well as commercially melted Nb-4at%Ta (Nb4Ta) and Nb-4at%Ta-1at%Hf (Nb4Ta1Hf) materials produced at substantial scale by ATI Specialty Alloys & Components. Our arc-melted alloys were fabricated in a Materials Research Corporation arc-melter in ultrahigh purity argon (Ar-UHP300) using commercial Nb4Ta alloy as the base to which Hf was added to obtain the ternary composition. The arc-melted ingots were prepared in batches of 30–50 g and had an ellipsoidal geometry with cross-sectional diameters of 4–7 mm and lengths of ~50–60 mm. Typically, more than 5 melting steps were used to ensure uniform mixing of the Hf alloy.

ATI Specialty Alloys & Components supplied the Nb4Ta and Nb4Ta1Hf as both rods (15 mm diameter, 400 mm length) and tubes (outer diameter 12.5 mm and thickness 2.5 mm). The received rods were annealed, with an average grain size of < 50 µm in both alloys. The Nb4Ta and Nb4Ta1Hf ingots had low reported interstitial levels of $<$ 0.005% O, $<$0.002%N, $<$0.003%C, and $<$0.0003%H. Initial ingot samples after melting were analyzed using a LECO Elemental Analyzer by the manufacturer, ATI Metals, for O, H, and N following the inert gas fusion technique. The samples are heated in a graphite crucible, and a mass flow controller measures the resulting CO_2 and H_2O to obtain the O, and H values, while the N is measured using a thermal conductivity detector[27]. No elemental analysis was performed on the lab-scale arc-melted alloys.

2.2. Fabrication and architectures of Nb4Ta1Hf and Nb4Ta multi-filament conductors

The schematic diagram in Fig. 1 shows the steps used to create a fine filament re-stack, rod in tube (RIT) conductor. By definition, a re-stack RIT conductor consists of a monofilament, as shown in Fig. 1a, b, stacked in a close packed scheme, with X elements in an outer Cu tube, Fig. 1c, and repeatedly drawn to decrease the conductor filament size. In each case, the monofilaments, starting with an initial cross-sectional area A_0, are drawn and hexed (Fig. 1c) and then stacked in a Cu tube, whose filament architecture follows an $X = 3\,n(n\text{-}1)+1$ configuration, where n is an integer (Fig. 1d shows a $n = 3$, $X = 19$ example). Further drawing, hexing (Fig. 1f), and restacking into a Y configuration (Fig. 1g) was then performed. After the restack, the conductor was further drawn to obtain filaments of reduced area A_{xy} (Fig. 1h). The true strain (ε) is calculated by the formula $\varepsilon = \ln(A_0/A)$, where A_0 and A are the initial alloy rod cross-sectional area and the final filament cross-sectional area respectively.

To evaluate and compare the strain drawability, Nb4Ta1Hf, Nb4Ta and Nb47Ti were first fabricated into monofilaments containing lab-scale and commercially obtained Nb alloys in a Cu matrix. Two different restack architectures were fabricated: a) 7 ×7 for the lab-scale alloys, and 19 ×19 in the case of the commercial alloys.

To study the quality of the Nb_3Sn produced from the Nb4Ta1Hf and Nb4Ta alloys, monofilaments were fabricated using a Sn-rod-cored alloy tube sleaved in a Cu tube. We designed them with a rather large Sn:Cu atomic ratio of 81:19 and they were drawn in a 19 × 1 design to a final wire diameter of 1 mm.

Table 1 details the components of the monofilaments fabricated for this study. The Cu tubing were sized based on the raw materials. For the drawability study, a Cu tube of outer diameter (OD) = 17.5 mm was used with the Nb4Ta1Hf and Nb4Ta alloys, whereas for the Nb47Ti the Cu tube OD was 12.5 mm. For the RIT Nb_3Sn, the inner Sn:Cu ratio was controlled by a Cu tube of OD 9.75 mm and an internal Sn rod with a diameter of 9.2 mm.

A 20% area reduction per drawing pass was used for the commercial alloys and the drawing speed was ~20–25 mm/min. For the arc-melted, and RIT conductors an area reduction of 10% per pass and a drawing speed of 5 mm/min was preferred. Variation of drawing speeds was not tested, and these parameters were selected considering our lab-scale equipment; further studies should be performed for industrial scale-up.

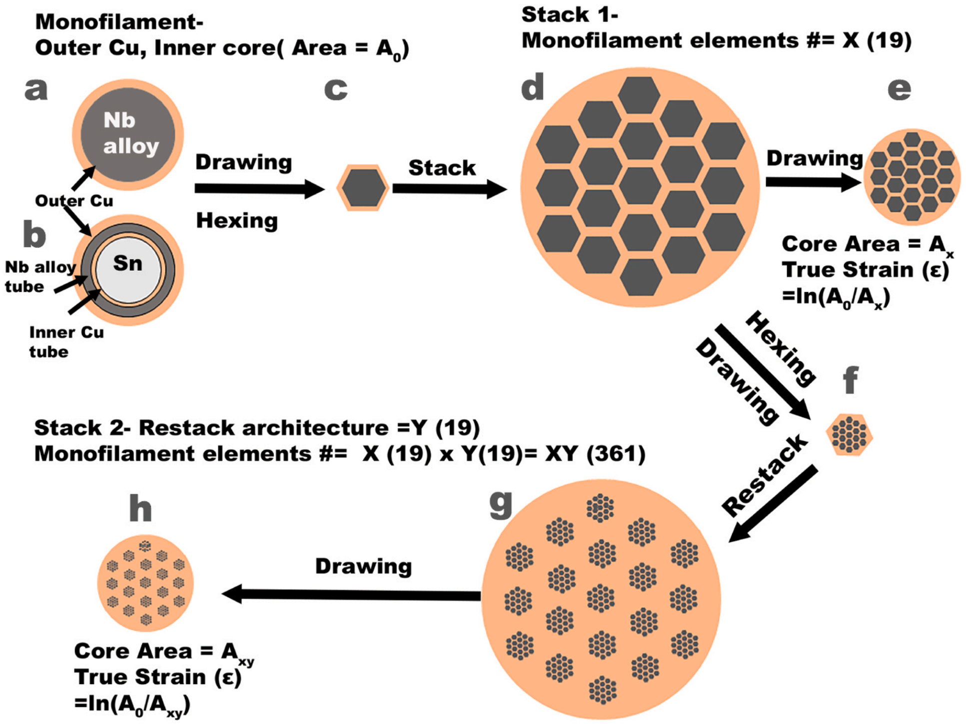

Fig. 1. Schematic of the restack process used to fabricate the X × Y composite multifilamentary conductors in this study. The initial monofilament stack is X, which is then restacked in an architecture Y, producing the final X × Y restacked conductors. For this example, X = 19 and Y = 19, and the total number of filaments is 361. True strain is measured as $\varepsilon = \ln(A_0/A)$, with A_0 and A being the initial and as-drawn areas.

Table 1
Summary of the alloys and starting cross-section dimensions of the Nb alloys used in monofilaments.

Alloy	–	Source	Starting shape/ dimensions	Restack Architecture- X × Y
Nb4Ta1Hf		Lab-scale (arc-melted)	Ellipsoid/ a= 7 mm, b= 4 mm	7 × 7
Nb4Ta			Ellipsoid/ a= 6 mm, b= 5 mm	7 × 7
Nb4Ta1Hf		Commercial, ATI	Rod/ ϕ = 15 mm	19 × 19
Nb4Ta				NA
Nb47Ti			Rod/ ϕ = 10 mm	19 × 19
Nb4Ta1Hf, Nb4Ta			Tube/ ϕ = 12.5 mm, t = 2.5 mm	19 × 1

2.3. Sample mounting, polishing procedures, microscopy and hardness measurements

The wires were hot-mounted in a conductive thermosetting mount, and then polished using standard metallographic techniques. Initial microstructures were revealed by grain boundary etching of the polished alloy cross-sections in a 1:1:2=HF: HNO_3:Lactic acid volumetric ratio solution. Grain size measurements were performed using the mean linear intercept method described in the ASTM-E112 standard [28].

A LECO-300 AT Vickers microhardness indenter was used with a typical load of 300 g (10 g were used only for the smallest filament diameter) and a dwell time of 15 sec to evaluate the hardness on polished cross-sections.

Electron microscopy was performed in a Zeiss 1540 EsB FESEM using a 4-quadrant solid-state backscattered electron detector. EDS measurements were performed at 15 kV, 1 µm spot width, and 100 nm line width settings using an EDAX Apollo XPP SDD detector.

2.4. Heat treatments

Heat treatments of the wires at a true strain of 7 were performed in the temperature range of 200 °C −900 °C, using the measured hardness to evaluate the onset of recrystallization. Extended heat treatment times of 50 and 100 h were added in the typical temperature range of the A15 reaction, 600 °C-700 °C, to evaluate the alloy microstructure development during the A15 reaction. The RIT conductors were heat-treated at 550 °C/100 h + 670 °C/100 h.

2.5. Superconducting characterization

We measured Nb_3Sn conductors in fields up to 31 T, at the National High Magnetic Field Lab (NHMFL, Tallahassee). Making measurements in high fields enables us to evaluate the conductor performance in the conditions that are required for future accelerator magnets (> 15 T). Since the focus of this paper is to evaluate the mechanical properties and the wire feasibility, wire design, Sn content and heat treatment are not optimized for high I_c,. For this reason we measured the I-V characteristics at 4.2 K only to extrapolate the irreversibility field through the Kramer plot $f_k(\mu_0 H) \propto [I_c(\mu_0 H)]^{0.5} \cdot (\mu_0 H)^{0.25}$[29]. H_k is the field where the flux lines are completely de-pinned and I_c goes to zero (and also $f_k(\mu_0 H_k)=0$). The Kramer function is valid for sparse grain boundary pinning in alloyed multi-filament Nb_3Sn superconductors.

3. Results

3.1. Microstructure of the lab-scale arc-melted and commercial alloys

The transverse cross-sectional light microscope images in Fig. 2 compare the microstructures in the lab-scale arc-melted and commercial alloy ingots and rods. The grain sizes of the lab-scale alloys are 710 ± 50 µm for Nb4Ta1Hf and 2500 ± 600 µm for Nb4Ta. Commercial Nb4Ta1Hf and Nb4Ta, having undergone significant thermomechanical processing and recrystallization after melting, have a much smaller

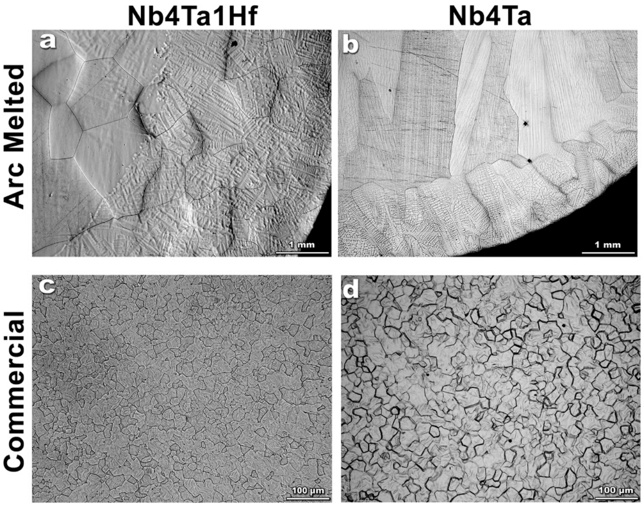

Fig. 2. Starting microstructures (light microscopy) of the Nb4Ta1Hf and Nb4Ta alloys used to fabricate conductors of this study. The in-house, lab-scale arc-melted alloys, Nb4Ta1Hf (a) and Nb4Ta (b) have large average grain sizes of 0.71 ± 0.05 mm and 2.5 ± 0.6 mm. The commercially obtained annealed rods have fine grain sizes of 31 ± 3 µm in the Nb4Ta1Hf alloy and 47 ± 2 µm in Nb4Ta.

equiaxed grain size, 31 ± 3 µm for Nb4Ta1Hf and 47 ± 2 µm for Nb4Ta. The backscattered electron (BSE) image of the Nb4Ta1Hf alloys in Fig. 3 shows that fine precipitates, seen as bright contrast, are present both in the lab-scale and the commercial alloys. They are lower in density, finer, and principally at the GBs in the lab-scale Nb4Ta1Hf alloy (Fig. 3a) while being higher in density, more uniformly distributed, and intra-granular in the commercial alloy (Fig. 3b). Point spectra of the large precipitates analyzed by EDS indicate the presence of Nb, Ta, Hf and O. Precise EDS analysis of the precipitates were limited by spatial EDS resolution. The brightness of the precipitates in the BSE image indicates the presence of high atomic number alloy elements which could be Hf or Ta and their absence in the Nb4Ta base alloy, suggests them to be Hf rich.

3.2. Drawability of Nb4Ta1Hf and Nb4Ta in multi-filament restack conductors

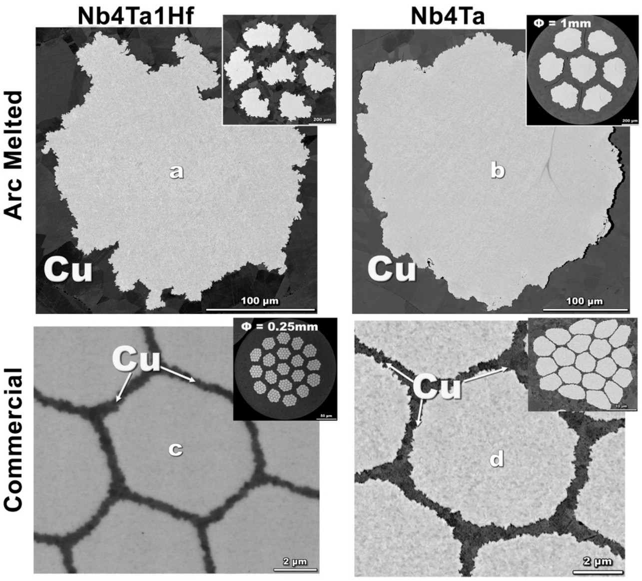

Fig. 4. Representative BSE images of Nb4Ta1Hf and Nb4Ta filaments in the fabricated composites. a) and b) are cross-sections of lab-scale Nb4Ta1Hf and Nb4Ta at $\varepsilon = 7.7$ and 7.2, respectively. c) and d) are transverse cross-sections of multi-filament conductors made with commercial Nb4Ta1Hf and Nb4Ta alloys at a strain of 15. Note the important differences in the alloy-Cu interfaces of the laboratory and commercial Nb alloys. A much smoother interface is obtained with the fine-grain, commercial Nb alloys.

Fig. 4 illustrates the impact of co-deformation of the various alloys in Cu matrices on their macrostructures. The lab-scale alloys with large grain size deform quite non-uniformly, as indicated by the jagged interface in the 325 µm diameter filaments in Fig. 4(a-b). Fig. 4(c-d) shows the fine grain commercial alloys drawn to smaller filament diameters of 6–7 µm, approaching large strain values of 15. The interface between commercial Nb alloys and Cu matrix is much smoother. The hexagonal shape of the Nb filaments is very well retained during the drawing of the commercial alloys. Table 2 summarizes the drawability experiments. The initial and final alloy area in Table 2, correspond to the initial cross-sectional area of the alloy rod in the starting monofilament, and the final cross-sectional area in the drawn wire as determined by image analysis. The main result is that commercial Nb4Ta1Hf and Nb4Ta with starting recrystallized grain sizes of less than 50 µm had excellent co-deformability with Cu to strains of 15 or more.

The hardness as a function of true strain for the Nb alloys is plotted in Fig. 5. The hardness of Nb4Ta1Hf (($HV_{0.3} \sim 70$–80) is always higher than in Nb4Ta ($HV_{0.3} \sim 55$–65) in the annealed state and at every strain level. The work hardening rate in the linear true strain (ε=2–11) region of the arc-melted Nb4Ta alloy is 12.7 $HV_{0.3}/\varepsilon$, whereas the Nb4Ta1Hf is slightly lower at 10.1 $HV_{0.3}/\varepsilon$. The commercial Nb4Ta work hardens at

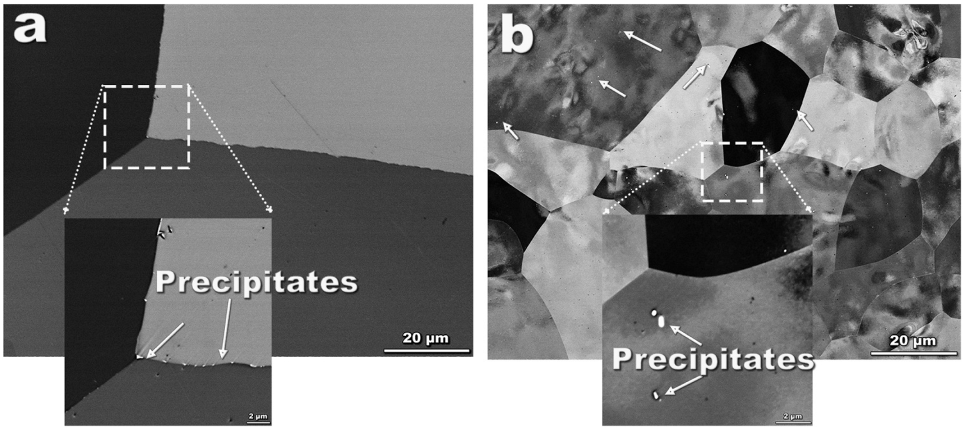

Fig. 3. BSE images for (a) lab-scale, arc-melted and (b) commercial Nb4Ta1Hf alloy-based wire show Ta/Hf rich precipitates. In (a) precipitates can be seen concentrated at grain boundaries, whereas in (b) the precipitate density is higher and they are distributed throughout the microstructure.

Table 2
Summary of the drawability of Nb4Ta1Hf, Nb4Ta alloys in a Cu matrix.

Alloy	Source	Initial grain size (μm)	Initial alloy area, A_0 (mm^2)	Restack Architecture- X × Y	Final alloy area, A_f (μm^2)	True Strain, $\varepsilon = \ln(A_0/A_f)$	Strain Hardening (Hollomon) $\sigma = K{\cdot}\varepsilon^n$	
							K (HV)	*n*
Nb4Ta1Hf	Lab-scale (arc-melted)	710 ± 500	88.7	7 × 7	NA	10.1*	124	0.39
Nb4Ta		2500 ± 600	94.5	7 × 7	NA	9.5*	100	0.42
Nb4Ta1Hf	Commercial ATI	31 ± 3	176.7	19 × 19	62 ± 2	14.9^+	101	0.34
Nb4Ta		47 ± 2	176.7	NA	36 ± 2	15.4^+	89	0.31
Nb47Ti	Commercial ATI	NA	78.5	19 × 19	19± 2	15.3^+	87	0.44

*Strain before fracture of the lab-scale alloys. The strain at break for the lab-scale Nb4Ta1Hf alloy was 10.4, and that of Nb4Ta was 9.8.

$^+$Wire drawing was stopped at strains of ~15. No breakages were observed in the commercial wires.

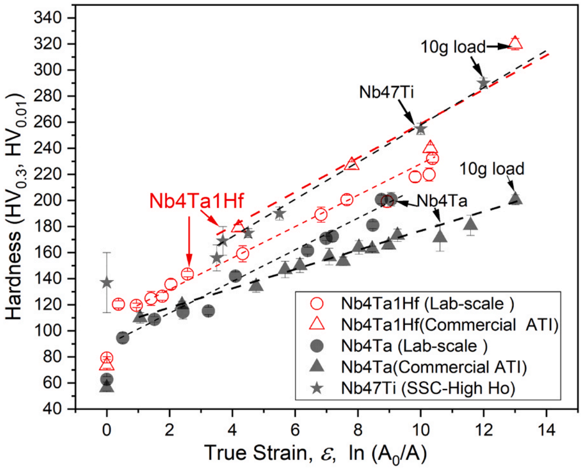

Fig. 5. Hardness as a function of true strain for Nb4Ta1Hf and Nb4Ta alloys evaluated in restacked and drawn composites. The hardness versus strain trend for Nb4Ta1Hf and Nb4Ta lab-scale, arc-melted alloys is similar in the explored strain range with Nb4Ta1Hf being consistently ~20 points higher than Nb4Ta. The commercial Nb4Ta alloy has a lower hardening rate than the commercial Nb4Ta1Hf alloy.

the lowest rate $7HV_{0.3}/\varepsilon$., while commercial Nb4Ta1Hf, and Nb47Ti work harden at similar rates of $15.7HV_{0.3}/\varepsilon$. Commercial alloy at $\varepsilon = 13$ has a hardness $HV_{0.01} = 320$, significantly higher than the 200 hardness of the commercial Nb4Ta alloy. The hardening behavior of the Nb4Ta1Hf commercial alloy corresponds more closely to the Nb47Ti alloy than the Nb4Ta alloy.

Strain hardening is generally expressed by the Hollomon equation relating flow stress and plastic strain:

$$\sigma = K \bullet \varepsilon^n \tag{1}$$

where σ is the flow stress or hardness, K is the strength coefficient with the same units as hardness, ε is the plastic strain, and *n* is the strain hardening exponent. The strain hardening exponent, *n*, of the various alloys calculated in the range of ε >4 is presented in Table 2. The commercial Nb alloys have lower *n* than their arc-melted counterparts. The *n* of commercial Nb4Ta is 0.31, and Nb4Ta1Hf 0.34, indicating that the higher starting hardness of the Nb4Ta1Hf alloy does not significantly change the strain hardening rate. The *K* values for Nb4Ta1Hf alloy are higher than the Nb4Ta alloy in all conditions. The *n* value of 0.44 for the Nb47Ti alloy is the highest in the alloy set considered. The *n* value of the Nb4Ta1Hf is similar to Nb4Ta, and much lower than that of highly drawable, much harder Nb47Ti.

3.3. *Recrystallization behavior of Nb4Ta1Hf, and Nb4Ta alloys*

To understand the effect of the Hf addition on the recrystallization behavior, we evaluated the hardness as a function of the heat treatment temperature at a strain of ~7 (Fig. 6) for 3 h holds at different temperatures. We found that Hf significantly shifts to higher temperature the steep drop in hardness seen as temperature is increased. The Nb4Ta alloy shows a sudden drop in hardness above 750 °C, whereas the Nb4Ta1Hf hardness decreases more gradually up to 900 °C.

In Fig. 6, we have also included data points for hardness measured on Nb4Ta1Hf and Nb4Ta alloys after holds at 50 h and 100 h. There is a slight decrease in hardness after the long-term holds of 50–100 h in both the Nb4Ta1Hf and Nb4Ta alloys.

Fig. 7 shows some examples of the microstructure of the two alloys after 3 h heat treatment at 650 °C-750 °C. The grains in the Nb4Ta alloy are polygonal, signifying recrystallization and grain growth. The grain size of Nb4Ta after 650 °C/3 h is 0.3±0.05 μm, growing to 7.0 ± 0.2 μm at 750 °C/3 h. The Nb4Ta1Hf grains (Fig. 7d-f) in the same temperature range remain elongated, showing retention of their cold-worked microstructure. The grain size calculated in the Nb4Ta1Hf alloy after 650 °C/3 h, and 750 °C/3 h is 0.12 ± 0.06 μm and 0.13 ± 0.02 μm, respectively.

In Fig. 8, we plot the grain size as a function of heat treatment temperature over a wider temperature range. The Nb4Ta1Hf alloy grain size after a 650 °C-800 °C/3 h heat treatment does not vary significantly and is 0.12 ± 0.02 μm, very similar to the as-deformed grain size. Beyond 800 °C, the grains in Nb4Ta1Hf show some growth to 0.32±

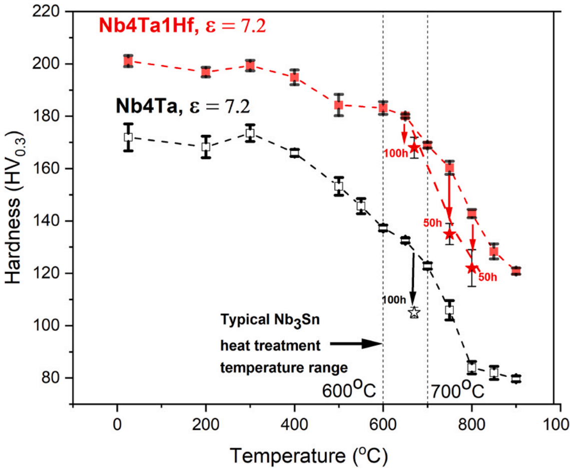

Fig. 6. Hardness as a function of heat treatment temperature for commercial Nb4Ta and Nb4Ta1Hf after a 3-hour heat treatment in the 23 °C - 900 °C range. For comparison, we also show the hardness evaluated on the Nb4Ta1Hf alloy (★) and Nb4Ta (☆) after much longer heat treatments (50–100 hours).

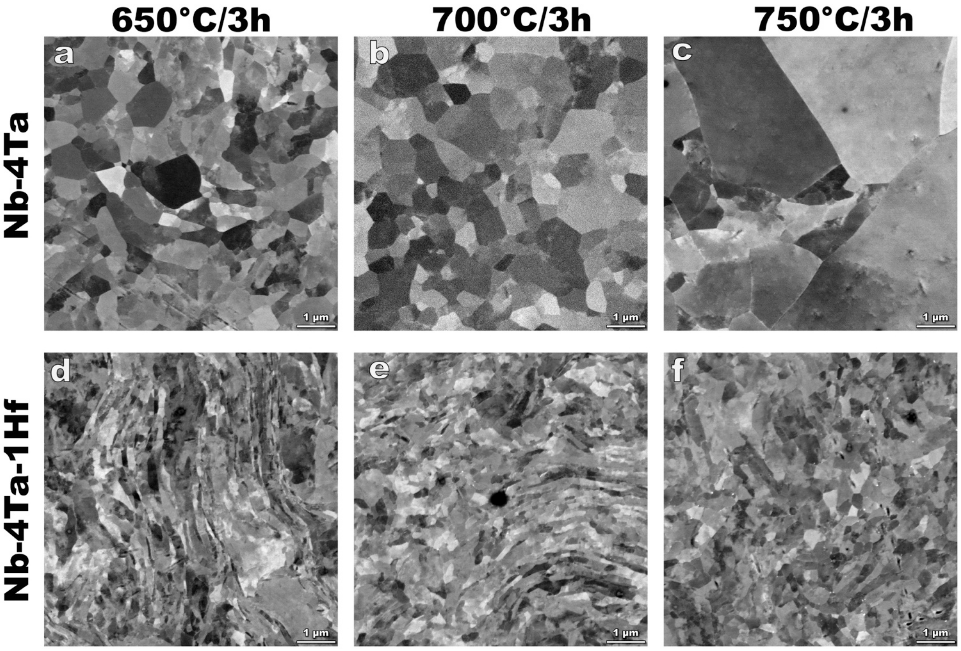

Fig. 7. Microstructure development (as observed by diffraction contrast in SEM-BSE imaging) for 3 h heat treatments at 650 °C, 700 °C, and 750 °C at a true strain of 7.2 in lab scale Nb4Ta (a-c), and Nb4Ta1Hf (d-f) alloys. The grain morphology of the Nb4Ta1Hf (d-f) shows longer retention of the worked microstructure and some grain growth, contrasting with the Nb4Ta, which shows significant grain growth.

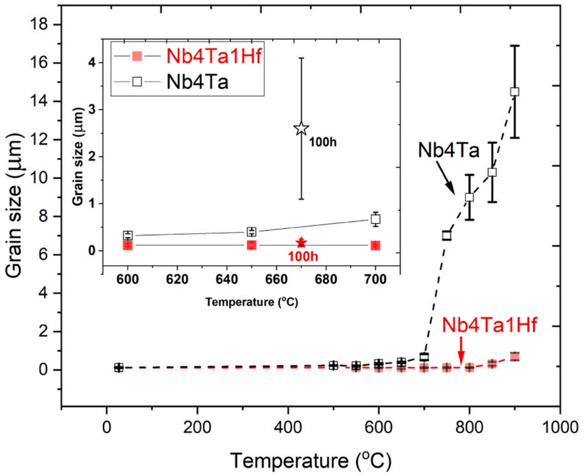

Fig. 8. Grain growth behavior as a function of temperature is shown for lab-scale Nb4Ta1Hf and Nb4Ta indicating grain growth occurs in the Nb4Ta alloy after a 650 °C/3 h heat treatment, whereas grain growth is fairly limited in Nb4Ta1Hf alloy even after a 900 °C/3 h heat treatment. The insert shows grain growth characteristics of the alloys within the temperature range of typical Nb_3Sn reactions. Some data for longer heat treatments are also shown (★, ☆).

0.10 μm after 850 °C/3 h and to 0.7 ± 0.20 μm after 900 °C/3 h. For Nb4Ta, grain growth starts at lower temperatures. After 600 °C/3 h, the grain size is 0.22 ± 0.01 μm, greater than the as-worked grain size of 0.12 ± 0.03 μm. Grain growth, with an average grain size of 0.3–0.4 μm is observed in Nb4Ta after 650 °C/3 h- 700 °C/3 h. However, after 750 °C/3 h, the grain growth is rapid and reaches 7.0 ± 0.2 μm. After longer heat treatment (100 h) the grain size of Nb4Ta at 670 °C is 2.6 ± 1.5 μm, much larger than the 0.17 ± 0.08 μm found for Nb4Ta1Hf.

We compare the alloy grain sizes in a RIT-19×1, where the Nb alloy undergoes a total strain of 8.8, after a 670 °C/ 50 h heat treatment. The micrograph in Fig. 9 compares the grain growth after the Nb_3Sn reaction in a 19×1 RIT conductor fabricated using the commercial Nb alloy tubes. Also, at the higher strain and for longer heat treatment, the Nb4Ta1Hf alloy has a finer grain size than the Nb4Ta alloy. The average grain size in the Nb4Ta1Hf alloy is 0.26 ± 0.14 μm, whereas the Nb4Ta alloy is 1.06 ± 0.52 μm. The Nb4Ta1Hf is equiaxed, suggesting that recrystallization processes may already be active, but the grain sizes are four times smaller than in the Nb4Ta alloy. Precipitates of the order of 50–100 nm are observed in the Nb4Ta1Hf alloy microstructure, whereas there are no precipitates in the Nb4Ta case.

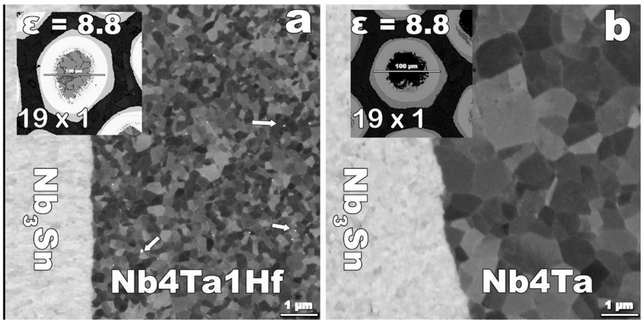

Fig. 9. BSE images of the interface between the Nb alloy and Nb_3Sn formed in a 19 × 1 RIT conductor after 670°C/50 h heat treatment in- a) Nb4Ta1Hf, and b) Nb4Ta alloy that have underwent a true strain of 8.8. The micrograph indicates a much finer grain size in the Nb4Ta1Hf as compared to the Nb4Ta counterpart.

In summary, hardness and grain size as a function of temperature indicate that adding 1 at%Hf suppresses recrystallization and grain growth in an Nb4Ta alloy. Moreover, Nb4Ta1Hf is fine-grained within the typical Nb_3Sn reaction window of 600 °C-700 °C, whereas Nb4Ta undergoes significant grain growth.

3.4. A15 properties of RIT conductors made with Nb4Ta and Nb4Ta1Hf alloys

RIT conductors fabricated in a 19×1 configuration were evaluated in transport in high fields to compare the irreversibility fields. Fig. 10

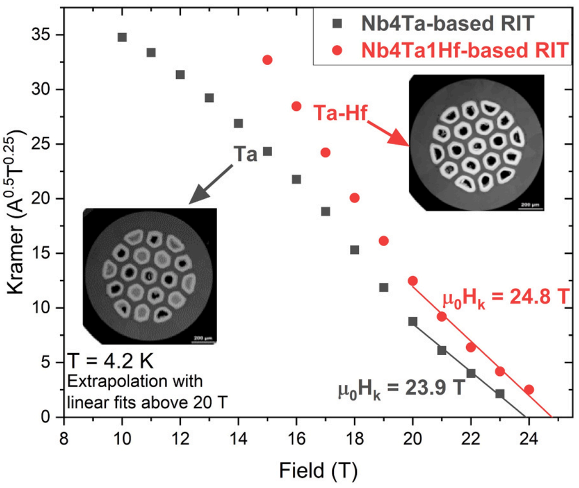

Fig. 10. Field dependence of Kramer plot at 4.2 K of Nb4Ta1Hf and Nb4Ta RIT-19 × 1 conductors after a 550 °C/100 h + 670 °C/100 h heat treatment. The curves were obtained from transport measurements in the 31 T resistive magnet at the NHMFL.

shows the Kramer plot of the wires made with Nb4Ta1Hf and Nb4Ta after a reaction heat treatment of 550 °C/100 h + 670 °C/100 h. The Kramer field, H_k(4.2 K), was estimated as 24.8 T for the NbTaHf-based conductor, ~1 T higher than in the Nb4Ta conductor (those H_k values, being determined only from the highest field data points, are a good evaluation of the irreversibility field, accordingly to ref.[30]). Since the reaction layer thickness was almost identical in the two wires (see the insets of Fig. 9 showing a similar level of reaction in the two wires) and the I_c(16 T) was more than 70% higher in the NbTaHf wire, we ascribe the difference to the intrinsically better performance of the Ta-Hf doped A15 phase.

Fractography was performed on the reacted RIT samples to evaluate the Nb_3Sn microstructures as indicated in (Fig. 11a-b). These images show that the Nb_3Sn grain morphology for the Nb4Ta1Hf wire is smaller and more equiaxed than for the Nb4Ta case. For Nb4Ta1Hf, the average grain size along the minor axis is 72 ± 13 nm, whereas for Nb4Ta is 102 ± 24 nm. A difference in the grain aspect ratio is also observed, being 1.55 in the Nb4Ta1Hf conductor and 2.0 in the case of Nb4Ta.

4. Discussion

4.1. Formability of Nb4Ta1Hf for Nb_3Sn internal Sn applications

Using these lab-fabricated multifilamentary composites, we have shown that commercially produced Nb4Ta1Hf is sufficiently ductile to be cold-drawn using standard wire drawing techniques to a strain of 15 without any wire breakage. Drawing of the Nb alloy in a Cu matrix is affected by the interface roughness especially when high Nb stacking density is desired. Large interface roughness leads to instability and breakages during large-strain conductor drawing [31]. However, especially in the Nb4Ta1Hf alloy, we have also observed a very low Cu-Nb interface roughness even at large strains. The interface roughness of Nb alloy drawn in a Cu matrix is affected by the initial grain size; the finer the initial grain size, the lower the interface roughness [32], [33], [34]. The industrial Nb4Ta1Hf alloy started with a grain size of less than 50 μm. It could be drawn to 5–6 μm filaments (Fig. 4c-d) with good shape retention of the hexagonal filaments despite significant hardening during wire drawing. Our experiments suggest that the strain hardening of commercial Nb4Ta1Hf is about twice that of Nb4Ta. However, the higher hardness of Nb4Ta1Hf is comparable to the Nb-47Ti alloy. For instance, at $\varepsilon = 10$, Nb47Ti has a hardness of 240 $HV_{0.3}$ [22], similar to commercial Nb4Ta1Hf in this study. The hardness of Nb4Ta at a similar strain is 160 $HV_{0.3}$.

Hf forms a substitutional solid solution with Nb, increasing initial hardness. A somewhat surprising result is that the commercial Nb4Ta1Hf alloy also contains precipitates, as shown Fig. 3b. In principle precipitates can act as dislocation pinning and multiplication centers and increase the flow stress, which may explain the higher hardness of the commercial Nb4Ta1Hf alloy. From the micrographs, precipitates in

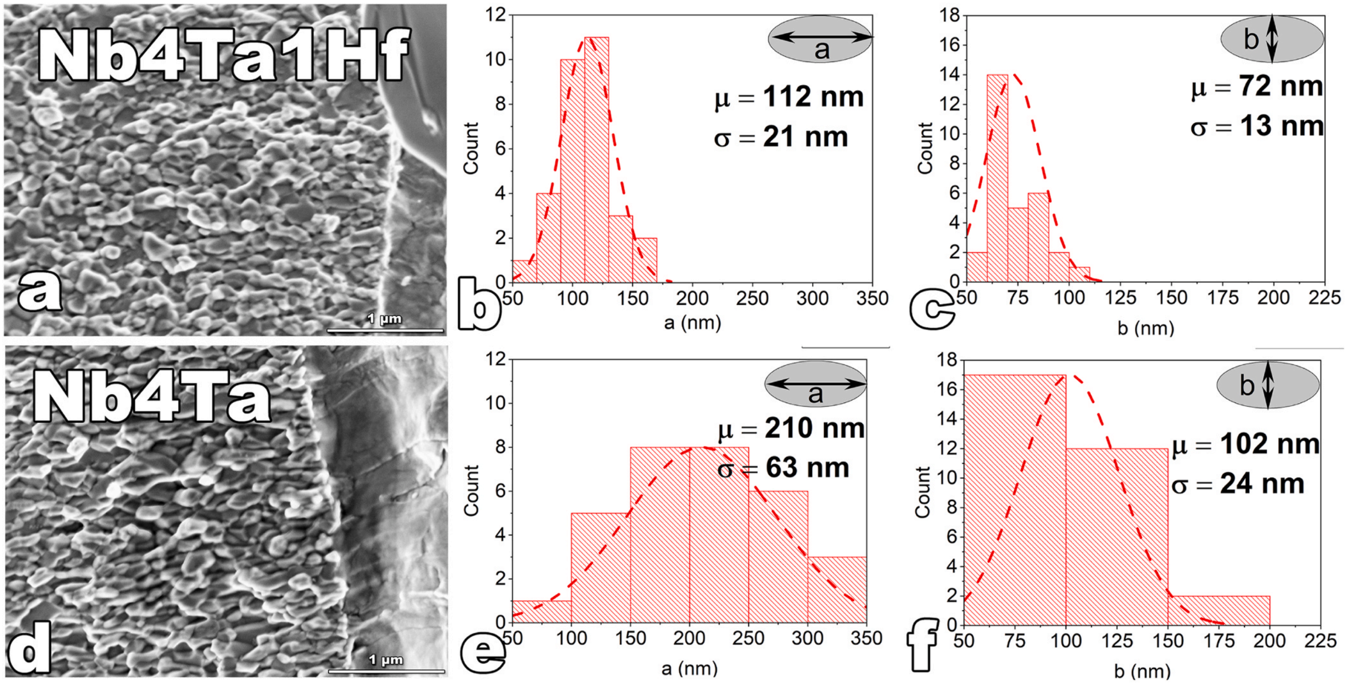

Fig. 11. Microstructure of Nb_3Sn in a 19 × 1 RIT conductor after 550 °C/100 h + 670 °C/100 h reaction heat treatment and transport measurement, a), d) are fractographs (FE-SEM in-lens SE) and (b), (c) and (e), (f) are grain size histograms measured as major a and minor diameters b of an ellipse for NbTaHf and NbTa respectively.

the arc-melted lab-scale alloys are restricted to the grain boundaries and are finer in size. In commercial alloys the precipitates are dispersed in the matrix, and the size and numbers are possibly related to the processing steps. Further analysis of the Hf rich precipitates is on-going. We expect a NbTaHf alloy with no precipitates to have lower hardness with strain.

The strain hardening exponent of the arc-melted Nb alloys is higher than that of commercial alloys: This result may indicate that arc-melted alloys have a higher interstitial content (N, O) than their commercial counterparts. In fact, in Nb alloys, the interstitial N or O can change the flow stress behavior and hardening exponent [35], [36].

4.2. Effect of Hf alloying on the recrystallization behavior of Nb alloy

Adding 1 at%Hf to the Nb4Ta alloy increases the recrystallization temperature by ~100 °C-150 °C, when the total strain in the alloy is ~7. The cold-worked Nb4Ta1Hf alloy has a finer grain size of ~120 nm while retaining the cold-worked structure (Fig. 8), whereas the Nb4Ta alloy grain size increases to several microns in the temperature and time range of 650 °C/3 h to 800 °C/3 h. When the total strain in the conductor increases to ~9, we still observe a refined grain structure in the Nb4Ta1Hf alloy after a 670 °C/50 h (Fig. 9). Nevertheless, the polygonal grains suggest that recrystallization and grain growth processes are active in the Nb4Ta1Hf alloy. Fig. 9 shows that after the same heat treatment the NbTaHf alloy always has a lower grain size than the NbTa alloy.

Increasing the strain lowers the recrystallization temperature leading to less retained cold work in the material and grain growth. For true strains greater than 15 expected in the superconductor fabrication, we could expect a higher level of recrystallization and grain growth in both Nb alloys, but with the NbTaHf alloy having smaller grain size and hence higher GB density than NbTa alloy. The presence of the Hf solute leads to grain refinement, and an increase in Hf content could provide an additional tool to adjust the strain sensitivity of the recrystallization temperature. This microstructural stability is also observed with Nb-Zr alloys, where increasing the Zr content retains the ultrafine grain structure even after elevated heat treatments at 700 °C[37].

This finer alloy grain size during the reaction heat treatment in the NbTaHf leads to a higher GB density than in the NbTa alloy at the same temperature. This higher GB density correlated to finer Nb_3Sn grain size, as evidenced by the interface of the NbTaHf alloy rod and the recently formed Nb_3Sn (which can be seen in the fractography in Fig. 11). In addition to Hf alloying effects on raising H_{c2} [21], [24], which contributes to the 1 T increase of H_K, the refined Nb_3Sn grain size induced by Hf increases the vortex pinning properties as demonstrated by the I_c enhancement. The increase in recovery and recrystallization temperature and retarded grain growth by Hf alloying has also been independently demonstrated by Banno *et al.*, who also observed a finer grain Nb_3Sn with higher J_c and F_{pmax} [38]. It is interesting to note that the grain refinement by Hf was not systematically found in [23], [39]. Asai *et al.* recently gave a possible explanation[40] revealing that Hf is more effective at Nb_3Sn grain refinement effect under high Sn activity conditions. This presumably explains the different findings obtained in different wire designs. There may be additional benefits to adding Hf in Nb_3Sn conductors. Recent work comparing internally oxidized Nb4Ta1Hf and Nb4Ta1Zr showed that Hf is preferable because it produces finer precipitates, in the range of 1–5 nm, compared to 10 s of nm in the Zr case [24].

Similar recent experiments, also finding that Hf additions reduce the Nb_3Sn grain size, were simultaneously and independently conducted by other groups [25], [26].

5. Conclusions

Nb4Ta1Hf is a ductile alloy with excellent co-deformation characteristics in a Cu matrix for strains up to at least 15, when the starting grain size in the alloy is less than 50 µm, even though Hf addition increases the work-hardening with respect to Nb4Ta. Hf-rich precipitates were found in both the commercial and lab-scale alloys.

Adding only 1 at% of Hf is highly effective in increasing the recrystallization temperature and decreasing the grain size during the Nb_3Sn reaction heat treatment. The delayed recrystallization or reduced grain growth of the Hf-based alloy could provide better Sn diffusion paths and denser Nb_3Sn grain nucleation, resulting in <100 nm, so finer Nb_3Sn grains. Moreover, the increased GB density in Nb_3Sn in the NbTaHf-based conductor leads to 70% higher I_c than its Nb4Ta-based counterpart with no difference in the A15 layer thickness, demonstrating that the TaHf-doped A15 phase is intrinsically better.

CRediT authorship contribution statement

Shreyas Balachandran: Writing – review & editing, Writing – original draft, Investigation, Formal analysis, Conceptualization. **Benjamin Walker:** Writing – review & editing, Validation, Data curation. **Peter J. Lee:** Writing – review & editing, Validation, Supervision, Methodology, Investigation, Conceptualization. **William L. Starch:** Writing – review & editing, Resources, Investigation. **Chiara Tarantini:** Writing – review & editing, Visualization, Investigation, Formal analysis. **David C. Larbalestier:** Writing – review & editing, Supervision, Project administration, Funding acquisition, Conceptualization.

Declaration of Competing Interest

The authors declare that they have no known competing financial interests or personal relationships that could have appeared to influence the work reported in this paper.

Data availability

Data will be made available on request.

Acknowledgements

This material is partly based upon work supported by the US Department of Energy, Office of Science, Office of High Energy Physics under Award Number DE-SC0012083, and cooperative agreement KN2713 from CERN. This work was performed at the National High Magnetic Field Laboratory, which is supported by National Science Foundation Cooperative Agreement= DMR-1644779 (2018–22) and DMR-2128556 (2023-), and the State of Florida. The authors thank Jeff Parrell, Bruker OST for providing Nb4Ta precursors for our alloy melting and David Smathers of HC Starck (now Materion) and Matthew Carl of ATI Specialty Alloys & Components for many discussions about the successful commercial production of the Nb4Ta1Hf alloy for high-field Nb_3Sn strand manufacturing.

References

[1] L. Bottura, “Magnets for future high energy and high intensity hadron beams,” presented at the Workshop on Accelerator Magnet Superconductors, Archamps, France: CERN, Mar. 2004, pp. 3–19. [Online]. Available: 〈https://cds.cern.ch/record/960889/files/p3.pdf〉.

[2] D. Schoerling and A.V. Zlobin, Eds., Nb_3Sn Accelerator Magnets: Designs, Technologies and Performance. Springer Nature, 2019. doi: 10.1007/978-3-030-16118-7..

[3] M. Benedikt, A. Blondel, P. Janot, M. Mangano, F. Zimmermann, Future circular colliders succeeding the LHC, Nat. Phys. vol. 16 (4) (Apr. 2020), https://doi.org/10.1038/s41567-020-0856-2.

[4] L. Rossi and O. Brüning, “Introduction to the HL-LHC Project,” in The High Luminosity Large Hadron Collider, vol. Volume 24, 0 vols., in Advanced Series on Directions in High Energy Physics, no. Volume 24, vol. Volume 24., WORLD SCIENTIFIC, 2015, pp. 1–17. doi: 10.1142/9789814675475_0001.

[5] P. Ferracin, et al., The HL-LHC low-β quadrupole magnet MQXF: from short models to long prototypes, IEEE Trans. Appl. Supercond. vol. 29 (5) (Aug. 2019) 4001309, https://doi.org/10.1109/TASC.2019.2895908.

[6] S.I. Bermudez, et al., Status of the MQXFB Nb_3Sn quadrupoles for the HL-LHC, IEEE Trans. Appl. Supercond. vol. 33 (5) (Aug. 2023) 4001209, https://doi.org/10.1109/TASC.2023.3237503.

[7] M.B. Field, Y. Zhang, H. Miao, M. Gerace, J.A. Parrell, "Optimizing Nb_3Sn conductors for high field applications,", IEEE Trans. Appl. Supercond. vol. 24 (3) (Jun. 2014) 6001105, https://doi.org/10.1109/TASC.2013.2285314.

[8] A.V. Zlobin, et al., Development and first test of the 15 T Nb_3Sn dipole demonstrator MDPCT1, IEEE Trans. Appl. Supercond. vol. 30 (4) (Jun. 2020) 400805, https://doi.org/10.1109/TASC.2020.2967686.

[9] B. Bordini, et al., The bundle-barrier PIT wire developed for the hilumi LHC project, IEEE Trans. Appl. Supercond. vol. 27 (4) (Jun. 2017) 6000706, https://doi.org/10.1109/TASC.2016.2640760.

[10] B. Bordini, et al., "Nb_3Sn 11 T Dipole for the High Luminosity LHC (CERN)," in Nb_3Sn Accelerator Magnets: Designs, Technologies and Performance, in: D. Schoerling, A.V. Zlobin (Eds.), Particle Acceleration and Detection, Springer International Publishing,, Cham, 2019, pp. 223–258, https://doi.org/10.1007/978-3-030-16118-7_9.

[11] L.D. Cooley, A.K. Ghosh, D.R. Dietderich, I. Pong, Conductor specification and validation for high-luminosity LHC quadrupole magnets, IEEE Trans. Appl. Supercond. vol. 27 (4) (Jun. 2017) 6000505, https://doi.org/10.1109/TASC.2017.2648738.

[12] C. Sanabria, M. Field, P.J. Lee, H. Miao, J. Parrell, D.C. Larbalestier, Controlling Cu–Sn mixing so as to enable higher critical current densities in RRP® Nb_3Sn wires, Supercond. Sci. Technol. vol. 31 (6) (Apr. 2018) 064001, https://doi.org/10.1088/1361-6668/aab8dd.

[13] C. Sanabria, I. Pong, L.P. LaLonde, S. Prestemon, Further heat treatment optimizations for Nb_3Sn conductors: from wires to cables, IEEE Trans. Appl. Supercond. vol. 29 (5) (Aug. 2019) 6001104, https://doi.org/10.1109/TASC.2019.2899498.

[14] A. Ballarino, L. Bottura, "Targets for R&D on Nb_3Sn conductor for high energy physics,", IEEE Trans. Appl. Supercond. vol. 25 (3) (Jun. 2015) 6000906, https://doi.org/10.1109/TASC.2015.2390149.

[15] C. Tarantini, P.J. Lee, N. Craig, A. Ghosh, D.C. Larbalestier, Examination of the trade-off between intrinsic and extrinsic properties in the optimization of a modern internal tin Nb_3Sn conductor, Supercond. Sci. Technol. vol. 27 (6) (Apr. 2014) 065013, https://doi.org/10.1088/0953-2048/27/6/065013.

[16] R.M. Scanlan, W.A. Fietz, E.F. Koch, Flux pinning centers in superconducting Nb3Sn, J. Appl. Phys. vol. 46 (5) (May 1975) 2244–2249, https://doi.org/10.1063/1.321816.

[17] X. Xu, X. Peng, J. Rochester, J.-Y. Lee, M. Sumption, High critical current density in internally-oxidized Nb_3Sn superconductors and its origin, Scr. Mater. vol. 186 (Sep. 2020) 317–320, https://doi.org/10.1016/j.scriptamat.2020.05.043.

[18] X. Xu, et al., APC Nb_3Sn superconductors based on internal oxidation of Nb–Ta–Hf alloys, Supercond. Sci. Technol. vol. 36 (3) (Feb. 2023) 035012, https://doi.org/10.1088/1361-6668/acb17a.

[19] J. Rochester, M. Ortino, X. Xu, X. Peng, M. Sumption, The roles of grain boundary refinement and nano-precipitates in flux pinning of APC Nb_3Sn, IEEE Trans. Appl. Supercond. vol. 31 (5) (Aug. 2021) 8000205, https://doi.org/10.1109/TASC.2021.3057560.

[20] S. Balachandran, et al., Beneficial influence of Hf and Zr additions to Nb4at%Ta on the vortex pinning of Nb_3Sn with and without an O source, Supercond. Sci. Technol. vol. 32 (4) (Feb. 2019) 044006, https://doi.org/10.1088/1361-6668/aaff02.

[21] C. Tarantini, et al., Origin of the enhanced Nb_3Sn performance by combined Hf and Ta doping, Art. no. 1, Sci. Rep. vol. 11 (1) (Sep. 2021), https://doi.org/10.1038/s41598-021-97353-w.

[22] S. Balachandran, et al., Beneficial influence of Hf and Zr additions to Nb4at%Ta on the vortex pinning of Nb $_3$ Sn with and without an O source, Supercond. Sci. Technol. vol. 32 (4) (Apr. 2019) 044006, https://doi.org/10.1088/1361-6668/aaff02.

[23] G. Bovone, et al., Effects of the oxygen source configuration on the superconducting properties of internally-oxidized internal-Sn Nb_3Sn wires, Supercond. Sci. Technol. vol. 36 (9) (Aug. 2023) 095018, https://doi.org/10.1088/1361-6668/aced25.

[24] X. Xu, et al., The strong influence of Ti, Zr, Hf solutes and their oxidation on microstructure and performance of Nb_3Sn superconductors, J. Alloy. Compd. vol. 857 (Mar. 2021) 158270, https://doi.org/10.1016/j.jallcom.2020.158270.

[25] C. Wang, et al., Influence of Hf addition on the superconducting properties of Nb_3Sn, IEEE Trans. Appl. Supercond. vol. 34 (3) (May 2024) 1–5, https://doi.org/10.1109/TASC.2023.3349258.

[26] N. Banno, T. Moronaga, T. Hara, K. Asai, T. Yagai, "In-depth S/tem observation of Ti–Hf and Ta–Hf-doped Nb_3Sn layers.", Aug. 17, Rochester, NY (2023), https://doi.org/10.2139/ssrn.4543590.

[27] "836 Series Elemental Analyzer," LECO Corporation. Accessed: Oct. 02, 2023. [Online]. Available: ⟨http://www.leco.com/product/836-series⟩.

[28] [Online] Accessed: Jan. 31 (2022). ⟨https://www.astm.org/e0112-13r21.html⟩.

[29] E.J. Kramer, Scaling laws for flux pinning in hard superconductors, J. Appl. Phys. vol. 44 (3) (Mar. 1973) 1360–1370, https://doi.org/10.1063/1.1662353.

[30] C. Tarantini, et al., Ta, Ti and Hf effects on Nb3Sn high-field performance: temperature-dependent dopant occupancy and failure of Kramer extrapolation, Supercond. Sci. Technol. vol. 32 (12) (Nov. 2019) 124003, https://doi.org/10.1088/1361-6668/ab4d9e.

[31] R.W. Heussner, P.J. Lee, P.D. Jablonski, D.C. Larbalestier, The influence of niobium and niobium-titanium grain size on the drawing instability of niobium diffusion barriers in niobium-titanium wire," in advances in cryogenic engineering materials: Volume 40, Part A, in: R.P. Reed, F.R. Fickett, L.T. Summers, M. Stieg (Eds.), in An International Cryogenic Materials Conference Publication, Springer US,, Boston, MA, 1994, pp. 755–762, https://doi.org/10.1007/978-1-4757-9053-5_96.

[32] S. Balachandran, et al., "Fine grained Nb for internal tin Nb_3Sn conductors," (Tuscon, AZ, USA), *AIP Conf. Proc.*, Trans. Int. Cryog. Mater. Conf. - ICMC: Adv. Cryog. Eng. Mater. vol. 1219 (Jul. 2009) 216–223, https://doi.org/10.1063/1.3402304.

[33] S. Balachandran, et al., Influences of different ECAE routes on filament deformation in Cu Clad Nb composite wires,", IEEE Trans. Appl. Supercond. vol. 21 (3) (2011) 2584–2587.

[34] S. Balachandran, D.B. Smathers, J. Kim, K. Sim, P.J. Lee, A method for measuring interface roughness from cross-sectional micrographs, IEEE Trans. Appl. Supercond. vol. 33 (5) (Aug. 2023) 6000205, https://doi.org/10.1109/TASC.2023.3250165.

[35] Z.C. Szkopiak, Flow stress of niobium-oxygen and niobium-nitrogen alloys,", J. Common Met. vol. 26 (1) (Jan. 1972) 9–17, https://doi.org/10.1016/0022-5088(72)90003-3.

[36] Z.C. Szkopiak, Oxygen dependence of strain-ageing in niobium, Acta Met. vol. 16 (3) (Mar. 1968) 381–391, https://doi.org/10.1016/0001-6160(68)90025-4.

[37] F. Rubitschek, T. Niendorf, I. Karaman, H.J. Maier, Microstructural stability of ultrafine-grained niobium–zirconium alloy at elevated temperatures, J. Alloy. Compd. vol. 517 (Mar. 2012) 61–68, https://doi.org/10.1016/j.jallcom.2011.11.150.

[38] N. Banno, T. Morita, T. Yagai, S. Nimori, Influence of parent Nb-alloy grain morphology on the layer formation of Nb_3Sn and its flux pinning characteristics, Scr. Mater. vol. 199 (Jul. 2021) 113822, https://doi.org/10.1016/j.scriptamat.2021.113822.

[39] C. Buehler, et al., Challenges and perspectives of the phase formation of internally oxidized PIT-Type Nb_3Sn conductors, IEEE Trans. Appl. Supercond. vol. 30 (4) (2020) 6000805, https://doi.org/10.1109/TASC.2020.2969906.

[40] K. Asai, T. Yagai, and N. Banno, "Effect of Hf Addition to Nb-alloy Core on Nb_3Sn Grain Morphology under the High Sn Diffusion Driving Force.," presented at the International Conference on Magnet Technology- MT 28, Aix-en-Provence, France, Sep. 14, 2023. Accessed: Dec. 03, 2023. [Online]. Available: ⟨https://mt28.aoscongres.com/⟩.